On Crack Opening Computation in Variational Phase-Field Models for Fracture

Keita Yoshioka[a,*], Dmitri Naumov[a,1], Olaf Kolditz[a,c]

[a] *Department of Environmental Informatics, Helmholtz Centre for Environmental Research – UFZ, Leipzig, Germany*
[b] *Chair of Soil Mechanics and Foundation Engineering, Technische Universitt Bergakademie Freiberg, Germany*
[c] *Applied Environmental Systems Analysis, Technische Universität Dresden, Dresden, Germany*

Abstract

Phase-field models for fracture have gained exceptional popularity in the last couple of decades and have been extended into areas well beyond brittle quasi-static fracture propagation to ductile, dynamic, or hydraulic fracturing. Despite the significant theoretical advancements in these more complex physical settings, little attention has been paid to the quantification of crack opening displacement to date as most applications do not explicitly require the crack opening displacement for the morphological evolution of cracks. However, one of the exemptions would be hydraulic fracturing where the crack propagation is driven by the fluid pressure which strongly depends on the crack opening displacement.

In this study, we look into two known approaches, a line integral and a level-set method, for crack opening computation mainly from an implementation point of view. Firstly, we derive an approximation of a discontinuous function field in the variational phase-field setting which is then applied to obtain the crack opening (displacement jump) and verify the approximation against a closed solution. We then propose a "certain distance from the crack" required for the level-set function using a one-dimensional analysis. Finally, we compare these approaches under several different conditions such as crack alignment to the mesh or under loading (asymmetric displacement field) and investigate the convergence with respect to the mesh size.

Keywords: crack opening displacement, fracture aperture, phase-field models of fracture, hydraulic fracturing, OpenGeoSys

1. Introduction

Phase-field models for fracture have become one of the standard numerical methods for fracture models since its initial introduction by Bourdin et al. [12, 13] as a regularisation model for the variational approach to fracture [23]. Their model for brittle and cohesive fracture has been further studied by many others [4, 6, 27, 34, 42, 50, 52, 57–59, 62] including advanced numerical solution schemes [22, 24]. In the last couple of decades, its application spans from ductile fracturing [2, 4, 35, 44] to fatigue [3, 54], desiccation fracture [16, 43], and dynamic fracturing [10, 14, 30, 41, 53].

*Corresponding author

Unlike external load driven fracturing, hydraulic fracture propagation is induced by the fluid pressure in crack whose geometry is then defined by the phase-field variable [1, 20, 36]. The first extension of the phase-field model to hydraulic fracturing has been proposed by Bourdin et al. [11] by regularising the work done by the fluid pressure within the cracks. Although in [11], the medium is considered as non-porous elastic, it is equivalent to consider a constant pore-pressure in an impermeable porous medium such as [48, 60, 64] in which the fluid does not leak off to the surrounding formation. Extension to a permeable porous medium with fluid leak-off is achieved through coupling with fluid flow models where Darcy flow in the porous medium and Reynolds flow in the crack are applied by Mikelić et al. [47, 49] and Miehe et al. [45, 46]. As the Reynolds flow model requires an explicit crack opening displacement, the crack normal displacement from the vicinity of cracked elements was used in these studies [17, 45–47, 49]. In [38, 39, 51], computation of the crack opening is obtained from a line integral originally presented by [11]. Lee et al. [40] proposed a level-set based approach for crack opening which has been also used in [55, 65]. Some other approaches that utilize Stokes flow instead of Reynolds flow in cracks [21, 28, 61] or simply modify the permeability in the Darcy model [63] do not require to resolve the crack opening. Instead, they need to explicitly identify in which domain which flow models (either Darcy or Stokes) should be applied and rely on an indicator function based on the phase-field variable.

Because of the Reynolds flow model's strong dependency on the crack aperture (the volumetric flow rate is proportional to the cube of the crack aperture), accurate resolution of the crack opening is essential. As it is reported in [19], however, crack opening computation in phase-field models is not straightforward. The first approach proposed for quantification of crack opening displacement (displacement jump) based the computation on the line integral utilising the gradient of the phase-field variable and has been verified against the now classical Sneddon's solution [56] in a quasi-static setting [11]. While in [60], the crack normal displacement in adjacent element has been shown to reproduce the crack opening obtained from the line integral, its justification and versatility are unclear. A comparison of the crack opening from the line integral against the Sneddon's solution in [48] shows a strong mesh size dependency, which seems to have been improved in [29] with adaptive mesh refinement. The mesh size dependency persists in another comparison by [40] using the level-set approach. Additionally, Chukwudozie et al. [18] has pointed out that implementation of the line integral method would require further special treatments in the identification of the crack normal direction and removal of spurious crack tip effects.

This paper is organised as follows. Section 2 briefly describes the mathematical formulation of the variational phase-field model for hydraulic fracturing in porous media and verifies the crack opening approximation computed by the line integral. In Section 3, the algorithms for the two approaches are shown. In Section 4, these two approaches are tested and compared in various scenarios to demonstrate their capabilities of reproducing the crack opening. Finally, conclusions are drawn in Section 5.

2. Technical background for variational phase-field models for fracture

2.1. Mechanical equilibrium

Our starting point is to consider a brittle-elastic porous medium whose constitutive law is denoted by $\mathbf{C}$ and the linearised strain as $\mathrm{e}(\vec{u}) := (\nabla\vec{u} + \nabla\vec{u}^{\mathrm{T}})/2$ with $\vec{u}$ denoting the displacement. Following Biot's poro-elasticity [9], the effective stress is $\sigma^{eff} := \sigma(\vec{u}) - \alpha p_p \mathrm{I}$ given the pore-pressure

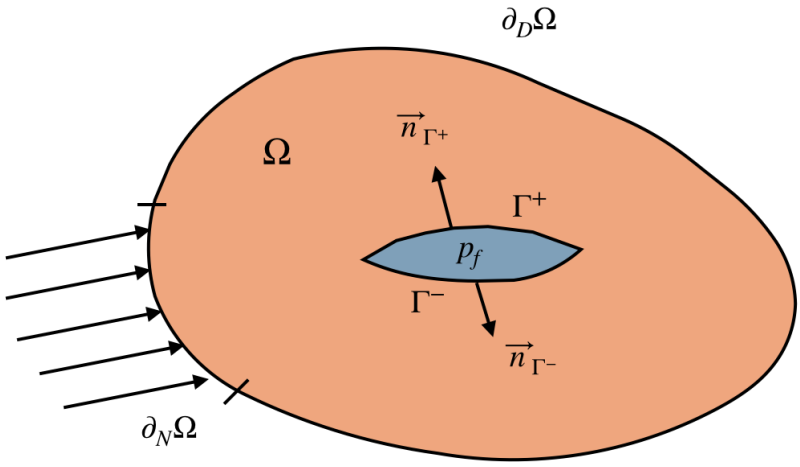

Figure 1: Brittle poro-elastic media with crack set Γ.

p_p and the Biot's coefficient of α. Then the strain energy density can be written as

$$W\left(\mathrm{e}(\vec{u}), p_p\right) := \frac{1}{2}\mathbf{C}\left(\mathrm{e}(\vec{u}) - \frac{\alpha}{N\kappa}p_p\mathrm{I}\right) : \left(\mathrm{e}(\vec{u}) - \frac{\alpha}{N\kappa}p_p\mathrm{I}\right), \tag{1}$$

where N is the dimension ($N = 1$, 2, or 3), and κ is the bulk modulus. With this strain energy density at hand, the potential for the medium depicted in Fig. 1 is expressed as [11]

$$\mathcal{P}(\vec{u}, \Gamma; p_p, p_f) := \int_{\Omega\setminus\Gamma} W\left(\mathrm{e}(\vec{u}), p_p\right)\, \mathrm{d}V - \int_{\partial\Omega_N^m} \vec{\tau}\cdot\vec{u}\,\mathrm{d}S - \int_{\Gamma} p_f\, [\![\vec{u}\cdot\vec{n}_\Gamma]\!]\, \mathrm{d}S - \int_{\Omega\setminus\Gamma} \vec{f}\cdot\vec{u}\,\mathrm{d}V, \tag{2}$$

where $\vec{\tau}$ is the traction force, the $\vec{f}$ is the body force, and p_f is the pressure in crack Γ. It should be noted that the pore-pressure is considered not continuous ($p_p \neq p_f$) on Γ.

With the consideration of crack set Γ and following the Francfort and Marigo's variational approach to brittle fracture [23], the total energy fo the system is given as:

$$\mathcal{F}(\vec{u}, \Gamma; p_p, p_f) = \mathcal{P}(u, \Gamma; p_p, p_f) + G_c \int_{\Gamma} \mathrm{d}S, \tag{3}$$

where G_c is the material's critical surface energy release rate. For a quasi-static process, resolving the displacement field reduces to minimizing $\mathcal{F}$ with respect to displacement $\vec{u}$ and crack set Γ.

Difficulties associated with the discontinuities in (3) can be alleviated through the now classical phase-field approach [11, 12]. By introducing a phase-field variable v which smoothly ranges from 0 (fully fractured) to 1 (intact) and a regularisation length parameter ℓ_s, the regularised form of (3) is given as:

$$\mathcal{F}_{\ell_s}(\vec{u}, v; p_p, p_f) = \int_{\Omega} W(\mathrm{e}(\vec{u}), v; p_p)\,\mathrm{d}V - \int_{\partial_N\Omega} \vec{\tau}\cdot\vec{u}\,\mathrm{d}S - \int_{\Omega} \vec{f}\cdot\vec{u}\,\mathrm{d}V - \int_{\Omega} p_f\,\vec{u}\cdot\nabla v\,\mathrm{d}V + \frac{G_c}{4c_n}\int_{\Omega}\left(\frac{(1-v)^n}{\ell_s} + \ell_s|\nabla v|^2\right)\mathrm{d}V, \tag{4}$$

where $n = 1$ and $n = 2$ correspond to a model known as $\mathtt{AT}_1$ and $\mathtt{AT}_2$ respectively, c_n is a normalisation parameter given by $c_n := \int_0^1 (1-\eta)^{n/2} \mathrm{d}\eta$, and $W(\mathrm{e}(\vec{u}), v; p_p)$ is a regularised strain energy density given as:

$$W(\mathrm{e}(\vec{u}), v; p_p) := \tfrac{1}{2} v^2 \mathbf{C} \left(\mathrm{e}(\vec{u}) - \frac{\alpha}{N\kappa}\, p_p \mathrm{I}\right) : \left(\mathrm{e}(\vec{u}) - \frac{\alpha}{N\kappa}\, p_p \mathrm{I}\right). \tag{5}$$

In arriving at (4) the following approximation [11, 18] is used

$$\int_\Gamma p_f \, [\![\vec{u} \cdot \vec{n}_\Gamma]\!] \, \mathrm{d}S \simeq \int_\Omega p_f \, \vec{u} \cdot \nabla v \, \mathrm{d}V. \tag{6}$$

Remark 1. *The regularised work done by the fluid pressure within the crack set Γ can be viewed as the body force $p_f \nabla v$ applied in the whole volume Ω.*

Note that the main driving force for crack propagation is p_f in the absence of the traction force $\vec{\tau}$ and that proper application of the fracture pressure p_f on the crack lips relies on its resolution of the crack normal $\vec{n}_\Gamma$ by ∇v. Also, the phase-field variable v that minimises (4) is no longer bounded in $[0, 1]$ even for $\mathtt{AT}_2$ because of the fracture pressure term, $p_f \, \vec{u} \cdot \nabla v$. Thus, solving of (4) requires a variational inequality solver, which is achieved via PETSc [7, 8] and the solution of (4) has been implemented in the open-source finite element framework OpenGeoSys [32, 33].

Initial cracks in phase-field models[1] are prescribed through the phase-field variable v by setting its value to 0 in the corresponding elements where cracks exist. The initial profile of v does not necessarily have a smooth profile and an optimal profile will be obtained once minimization of (4) is achieved (see the next subsection for the optimal profile construction).

2.2. Approximation of the crack opening

We follow the construction steps of the *optimal profile problem* in [13, 15], which is the construction of a function ω minimizing

$$\int_0^\infty \frac{(1-\omega)^n}{\ell_s} + \ell_s (\omega')^2 \, \mathrm{d}x =: \int_0^\infty S(x, \omega, \omega') \mathrm{d}x, \tag{7}$$

amongst all functions ω such that $0 \le \omega(x) \le 1$ on $(0, \infty)$, $\omega(0) = 0$, and $\omega(\infty) = 1$. The Euler-Lagrange equation to minimize the integral above is given by

$$\frac{\partial S}{\partial \omega} - \frac{d}{dx} \frac{\partial S}{\partial \omega'} = -\frac{n(1-\omega)^{n-1}}{\ell_s} - 2\ell_s \omega''. \tag{8}$$

For $\mathtt{AT}_1$ $(n = 1)$, we recover the well known optimal profile

$$\omega_1(x) = \begin{cases} 1 - \left(1 - \dfrac{|\xi|}{2\ell_s}\right)^2, & \xi \le 2\ell_s \\ 1, & \xi > 2\ell_s \end{cases} \tag{9}$$

[1] It can be defined as an explicit discontinuity if placed on the boundary. But it will be represented by the phase-field variable once crack propagation starts and this initial setting is known to produce inaccurate onset strength when compared to theories [31, 57].

and for $\mathtt{AT}_2$ ($n = 2$), it is

$$\omega_2(x) = 1 - e^{-|\xi|/\ell_s}, \tag{10}$$

where ξ is the distance from crack. Now consider a line crack that lies on $y = 0$ in 2D (i.e. $\xi = y$) and we wish to evaluate a variable $\phi(x, y)$ that includes a jump set across the crack. It can be shown that the magnitude of a jump set may be approximated from an integral, $\int_{-\infty}^{+\infty} \phi(x, y)|\nabla v(y)|\,\mathrm{d}y$. Introducing a variable $\tilde{y} = y/\ell_s$ the integral becomes

$$\int_{-\infty}^{+\infty} \phi(x, \ell_s\tilde{y})|\nabla v(y)|\,\mathrm{d}\tilde{y} = \int_{-\infty}^{0} \phi(x, \ell_s\tilde{y})|\nabla v(y)|\,\mathrm{d}\tilde{y} + \int_{0}^{+\infty} \phi(x, \ell_s\tilde{y})|\nabla v(y)|\,\mathrm{d}\tilde{y}. \tag{11}$$

As ℓ_s approaches 0,

$$\begin{aligned}\int_{-\infty}^{0} \phi(x, 0)|\nabla v(y)|\,\mathrm{d}\tilde{y} + \int_{0}^{+\infty} \phi(x, 0)|\nabla v(y)|\,\mathrm{d}\tilde{y} \\ = \phi(x, 0^-) \int_{-\infty}^{0} |\nabla v(y)|\,\mathrm{d}\tilde{y} + \phi(x, 0^+) \int_{0}^{+\infty} |\nabla v(y)|\,\mathrm{d}\tilde{y}.\end{aligned} \tag{12}$$

Using the optimal profile of v in (9) or (10), $\int_0^{+\infty} |\nabla v(y)|\,\mathrm{d}\tilde{y} = 1$. Therefore, we have

$$\int_{-\infty}^{+\infty} \phi(x, y)|\nabla v(y)|\,\mathrm{d}y \approx \phi(x, 0^+) - \phi(x, 0^-). \tag{13}$$

Following this result, a normal displacement jump over the crack Γ can be estimated as

$$\begin{aligned}\vec{u} \cdot \vec{n}_\Gamma(x, 0^+) - \vec{u} \cdot \vec{n}_\Gamma(x, 0^-) &\approx \int_{-\infty}^{+\infty} \vec{u} \cdot \vec{n}_\Gamma |\nabla v(y)|\,\mathrm{d}y \\ &\approx \int_{-\infty}^{+\infty} \vec{u} \cdot \nabla v(y)\,\mathrm{d}y,\end{aligned} \tag{14}$$

with the assumption of $\vec{n}_\Gamma(x, 0^+) = \vec{n}_\Gamma(x, 0^-)$ and the approximation of $\vec{n}_\Gamma \approx \nabla v(y)/|\nabla v(y)|$.

2.3. Verification of the crack opening computation

The approximation method proposed in (14) is for an infinite line crack that lies on $y = 0$ and its tip effects are not considered in the construction above. In this subsection, the proposed approach is tested against the well known closed form solution by [56] for a finite 2D line crack under the internal crack pressure, p. With an initial crack $\Gamma_0 = [-a, +a] \times \{0\}$ (Fig. 2), the closed form solution for crack opening displacement is given by

$$u_y^+(x, 0) = \frac{2pa}{E'} \left(1 - \frac{x^2}{a^2}\right)^{1/2}, \tag{15}$$

with $E' = E(1 - \nu^2)$ where E and ν are the Young's modulus and the Poisson's ratio respectively. Considering a square domain $\Omega = [-1, +1] \times [-1, +1]$ with a line crack $\Gamma_0 = [-0.1, +0.1] \times \{0\}$, an initial profile of v is specified as $v = 0$ for $[-0.1, +0.1] \times [-h/2, +h/2]$ accordingly where h is the element size. Fig. 3(a) shows the initial assignment of the phase-field variable for $h = 0.01$, which is the uniform quadrilateral element size in the subdomain $[-0, 3, +0.3] \times [-0.3, +0.3]$. As can be

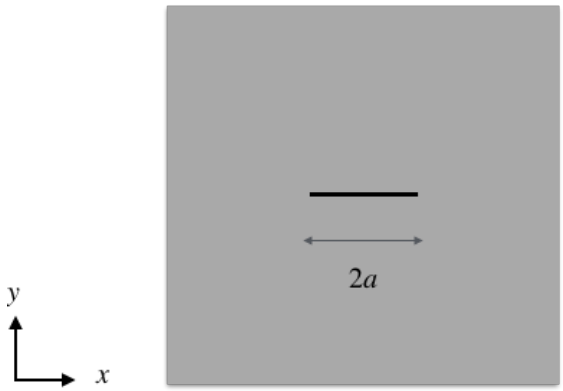

Figure 2: 2D line crack ($x = -a$ to $x = a$) with the half length of a under a constant pressure of p.

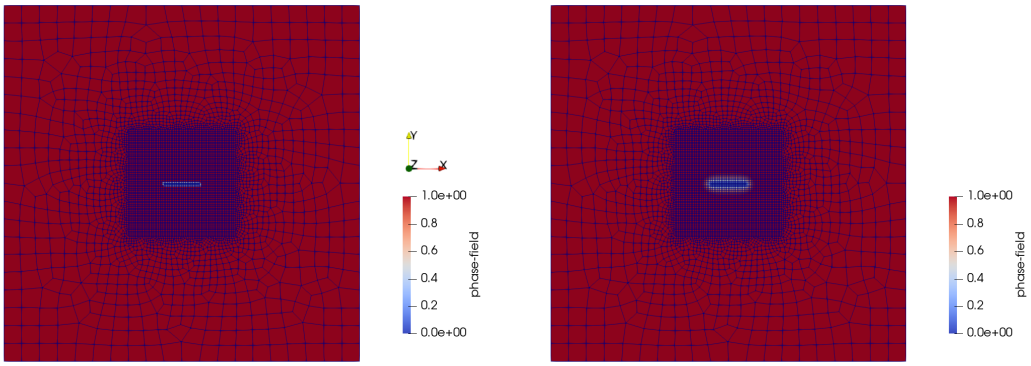

(a) Initial assignment of the phase-field variable

(b) Computed phase-field profield

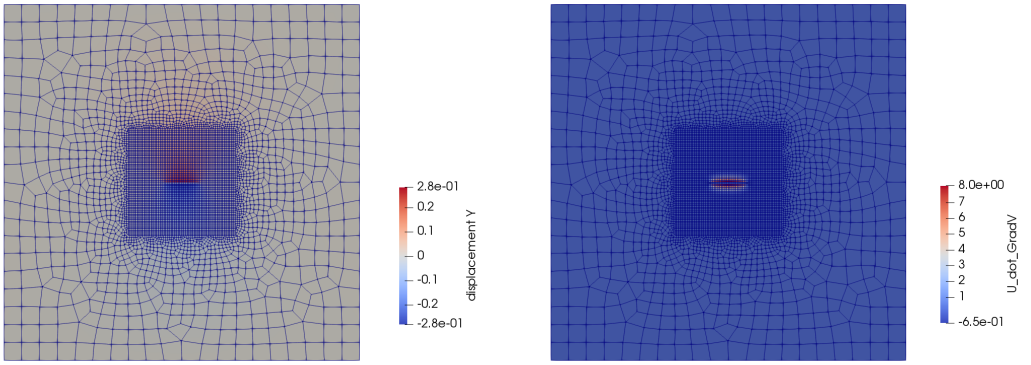

(c) Computed y-displacement

(d) Computed $u \cdot \nabla v$

Figure 3: Line integral of $u \cdot \nabla v$ from $y = +\infty$ to $y = -\infty$ performed post equilibrium computation of u and v.

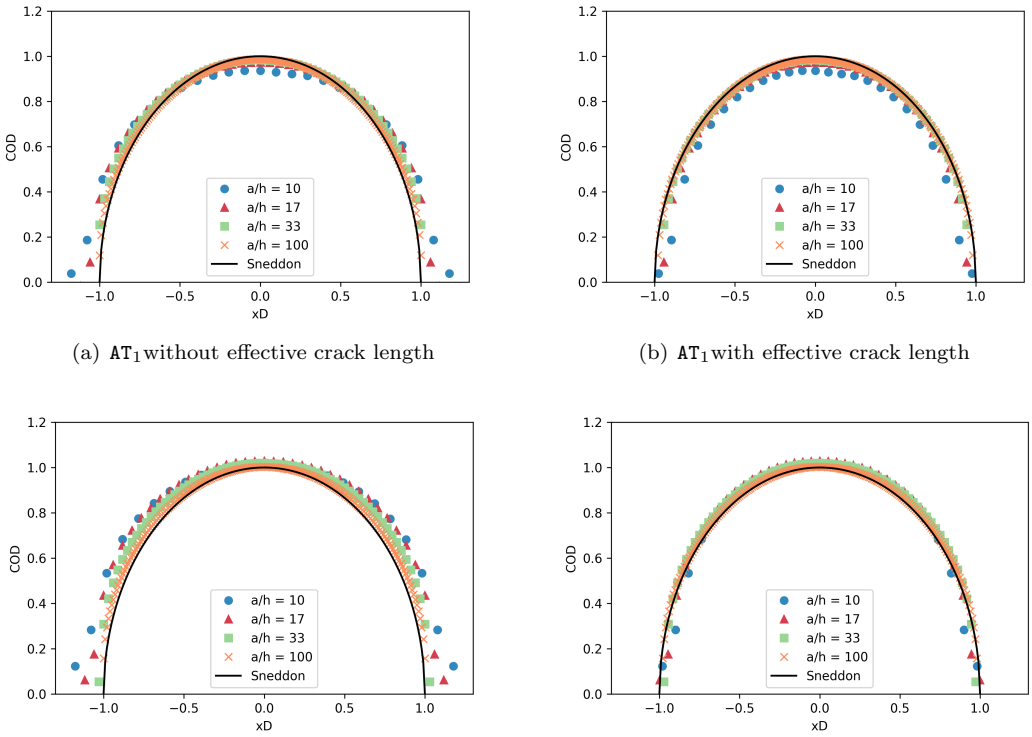

(a) $\texttt{AT}_1$ without effective crack length

(b) $\texttt{AT}_1$ with effective crack length

(c) $\texttt{AT}_2$ without effective crack length

(d) $\texttt{AT}_2$ with effective crack length

Figure 4: Results from line integral of $u \cdot \nabla v$ from $y = -1$ to $y = +1$ on various mesh resolutions ($a/h = 10$, $a/h = 17$, $a/h = 33$, and $a/h = 100$) compared against the closed form solution for $\texttt{AT}_1$ and $\texttt{AT}_2$ with and without effective crack length adjustment.

seen in Figs. 3, the elements outside of the subdomain consists of coarse quadrilateral and triangle elements. For a given pressure in crack ($p_f = 1.0$) and pore-space ($p_p = 0.0$), the mechanical properties of $E = 1.0$, $\nu = 0.15$, and $G_c = 1.0$, and the regularisation parameter of $\ell_s = 0.03$, displacement and phase-field variable profiles were identified by minimising (4). The computed phase-field profile and $y-$displacement are shown in Figs. 3(b) and 3(c). Using (14), a line integral of $u \cdot \nabla v$ (Fig. 3(d)) was taken in $[-1, 1]$ on various mesh resolutions ($a/h = 10$, $a/h = 17$, $a/h = 33$, and $a/h = 100$) for both $\texttt{AT}_1$ and $\texttt{AT}_2$ models. The results are compared against the closed form solution along $[-a, a] \times \{0\}$ in Figs. 4(a) and 4(c) respectively and x_D represents the normalised distance from the crack center as $x_D = x/a$. As reported by other studies [25, 29, 40], it shows strong dependencies on the mesh resolution especially near the crack tip and the results seem to converge to the closed-form solution as the mesh is refined. It is known that the effective fracture toughness in the variational phase-field setting increases by a factor that depends on the mesh size h and the regularisation length ℓ_s and is given as [13]

$$G_c^{\text{eff}} = G_c \left(\frac{h}{4 c_n \ell_s} + 1 \right). \tag{16}$$

In addition, its effective crack length needs to be taken into account when cracks are represented by the phase-field variable. The 2D line crack in consideration possesses the surface energy of $\frac{1}{4}G_c(2a)$ which is regularised to $\int_\Omega S(x, v, v')$. By equating these two energies (see Appendix for details), the effective crack length a^{eff} for $\texttt{AT}_1$ is estimated as:

$$a^{\text{eff}} = a\left(1 + \frac{\pi\ell_s}{4a(3h/8\ell_s + 1)}\right). \tag{17}$$

Similarly for $\texttt{AT}_2$, it is:

$$a^{\text{eff}} = a\left(1 + \frac{\pi\ell_s/4}{a(h/2\ell_s + 1)}\right). \tag{18}$$

The effective fracture toughness discussion can also be found in [13] and it is indeed dependent on the ratio of the element size to the regularisation length, which indicates that the material strength varies with the regularisation length. Thus, the fracture toughness used in computation always needs to be adjusted corresponding to the discretisation and the regularisation lengths. While the effective length too needs adjustment, it converges to the actual length as the regularisation length approaches to zero. With the effective crack lengths, the obtained solutions are compared again with the closed form solution in Figs. 4(b) and 4(d). Though some discrepancies still can be observed near the crack tip, overall matches against the closed form solution are improved significantly. Also, $\texttt{AT}_1$ model in general provides a better match because of its finite phase-field profile. Thus in the following we use $\texttt{AT}_1$ model for our analysis unless otherwise specified.

3. Approaches for computational implementation of crack opening

The crack opening computation by taking a line integral from $-\infty$ to $+\infty$ in the crack normal direction has been verified to reproduce the crack opening quite accurately in the previous section. In practical computation, however, two issues arise in this approach; 1) there could be multiple cracks in the path from $+\infty$ to $-\infty$, and 2) the crack normal direction may change along the integration path. In order to address these issues, two different approaches are considered. The first approach still utilizes a line integral but over a finite length [48, 51] following the local crack normal direction [18]. The second approach is to define a level-set function to infer the crack opening displacement from a certain point from the function [40, 65]. In this section, these two approaches are studied and compared in various conditions.

3.1. Line integral method

The first approach presented here is nearly identical to the procedure proposed in [18] where the line integral is carried out locally by following the local crack normal vector except for the termination criteria and the way crack tip effects are removed.

As shown in Fig. 5, the integral follows the crack normal vector computed at element using the gradient of the phase-field as $\vec{n}_{\Gamma,i} = \nabla v_i/|\nabla v_i|$. Its integration discontinues either when it exits the phase-field transition zone ($v_{j+1} < 1$) or it enters another crack's ($\vec{n}_{\Gamma,j+1} \cdot \vec{n}_{\Gamma,i} < 0$). Note that the first exit criterion is especially important for $\texttt{AT}_2$ where the phase-field profile is represented by an exponential function. The detailed procedures are described in Algorithm 1. An example of computed crack opening profile for an inclined crack (22.5° from the horizontal axis) is shown in Fig. 6(a), which exhibits non-zero crack openings beyond the crack tips. This is because the normal

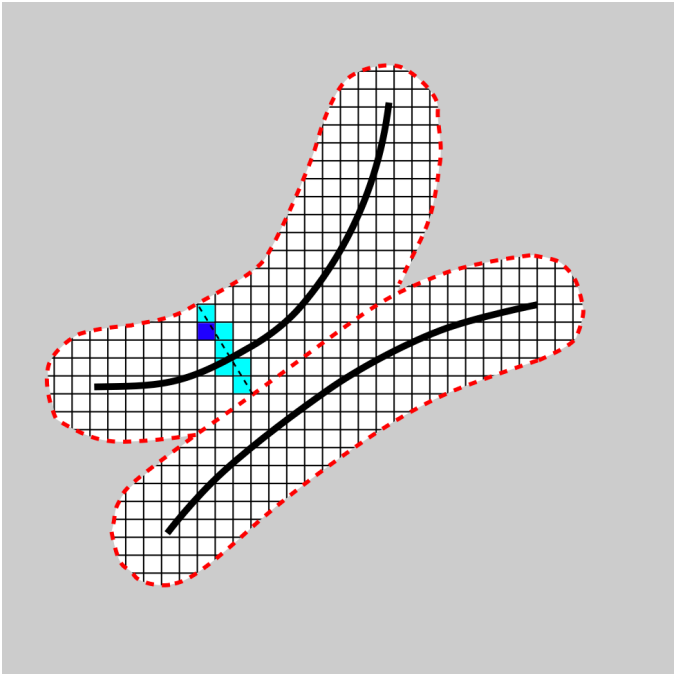

Figure 5: Schematic of local line integral method. The integration progresses in both directions (positive and negative crack normals along the dashed black line), starting from the reference element (highlighted in blue). The integration terminates either when it is out of the crack transition zone (gray) or enters another crack's regularisation region. The participating elements are highlighted in cyan.

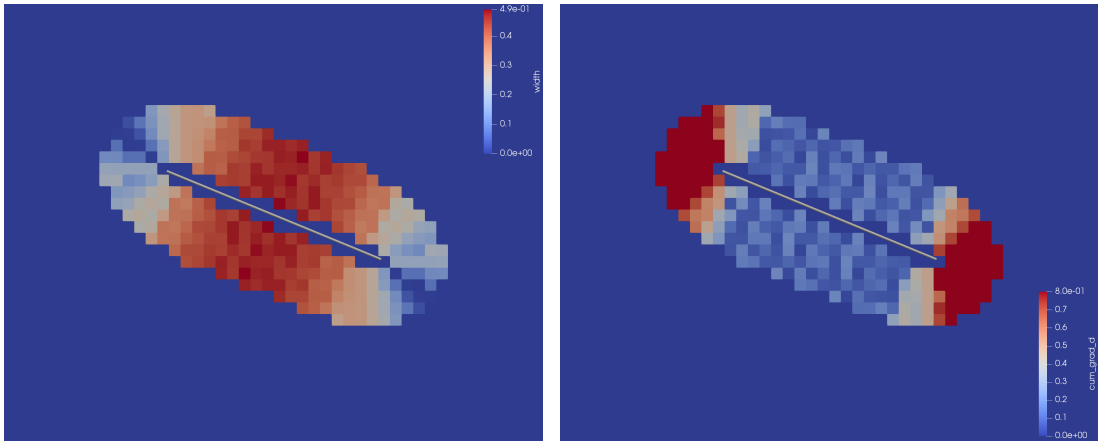

(a) Crack opening profile

(b) Integral of ∇v_i

Figure 6: Spurious crack opening around the crack tip. The white line indicates the actual location of the crack. The elements that are initially assigned with $v = 0.0$ are given with no width for illustration purpose.

direction to the crack is not clearly defined near the tip with finite discretisation. Although an integral of ∇v_i should result in $\vec{0}$ if $\vec{n}_\Gamma$ is orthogonal to Γ, it does not cancel out to $\vec{0}$ near crack tips due to the improper identification of the crack normal direction. Fig. 6(b) shows the magnitude of the sum of ∇v_i along the locally resolved crack normal direction. It can be observed that the sum is close to 0 where the crack normal direction is properly identified and deviates away from 0 in the vicinity of the crack tips, which leads to non-zero crack openings beyond the crack tips. In order to remove this unwanted tip effects, the crack opening is multiplied by the indicator function I_w ($w' = I_w w$), which is defined as:

$$I_w := \begin{cases} 1 & \text{if } |\sum_i \nabla v_i| \leq \delta_w, \\ 0 & \text{otherwise.} \end{cases} \tag{19}$$

where δ_w is a threshold for the error and 0.8 is found to be sufficient in this study. However, this value may differ if the line integral is evaluated differently and more systematic or universal method to estimate the threshold may be needed.

3.2. Level-Set method

The second approach studied is based on a level-set method originally proposed by [40] where identification of the crack opening displacement is performed using a level-set function. With the use of a linear level-set function, it is, in essence, identical to finding an equivalent displacement at some distance away from the crack lip as applied in [46, 47]. Fig. 7 compares the displacement profile in y-direction u_y at $x = 0$ from the previous section's example (Fig. 3) against the actual displacement profile computed using a discrete crack.

As can be seen in the vicinity of the crack in Fig. 7(b), the crack opening directly obtained from the phase-field computation at the crack lip would overestimate the actual opening displacement because neither displacement nor stress has a clear physical definition within the regularised region. Miehe et al. [46] suggested to read the crack normal displacement at certain characteristic length

Algorithm 1 Crack opening computation at the element e_i

Let v_i be the element average of v and $\vec{x}_i$ be the centroid coordinate of element e_i
Set $j = i$, $\vec{n}_{\Gamma,i} = \nabla v_i / |\nabla v_i|$, and $s = \text{sign}(\vec{n}_{\Gamma,i} \cdot \vec{n}_{\Gamma,j})$
while $v_{j+1} < 1$ or $\vec{n}_{\Gamma,j+1} \cdot \vec{n}_{\Gamma,i} \geq 0$ **do**
    Let $\vec{x}_{j+1} = \vec{x}_j + s \triangle l_\varepsilon \vec{n}_{\Gamma,j}$
    Identify the neighbor element, e_{j+1}, which contains $\mathbf{x}_{i+1}$
    if $\vec{n}_{\Gamma,j+1} = 0$ **then**
        $\vec{n}_{\Gamma,j+1} = \vec{n}_{\Gamma,j}$ // Continue in the same search direction
    else if $\vec{n}_{\Gamma,j+1} \cdot \vec{n}_{\Gamma,j} < 0$ **then**
        $\vec{n}_{\Gamma,i} = -\vec{n}_{\Gamma,i}$ // Flip the search direction
        $s = \text{sign}(\vec{n}_{\Gamma,i} \cdot \vec{n}_{\Gamma,j})$
    $w = w + \triangle l_\varepsilon (\vec{u}_j \cdot \nabla v_j + \vec{u}_{j+1} \cdot \nabla v_{j+1})/2$ // Line integral
Set $j = i$, $\vec{n}_{\Gamma,i} = -\nabla v_i / |\nabla v_i|$ and $s = \text{sign}(\vec{n}_{\Gamma,i} \cdot \vec{n}_{\Gamma,j})$
while $v_{j+1} < 1$ or $\vec{n}_{\Gamma,j+1} \cdot \vec{n}_{\Gamma,i} \geq 0$ **do**
    4–11

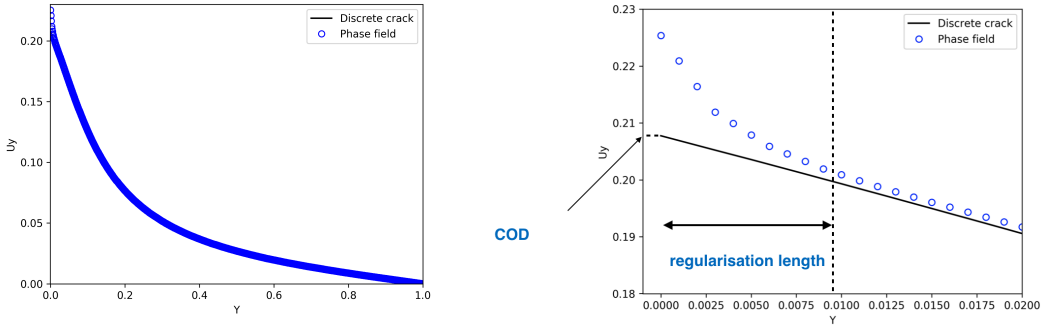

(a) Computed results over the entire computation domain

(b) Computed results near the crack

Figure 7: Comparison of computed displacement profile in y-direction from phase-field and discrete crack representations.

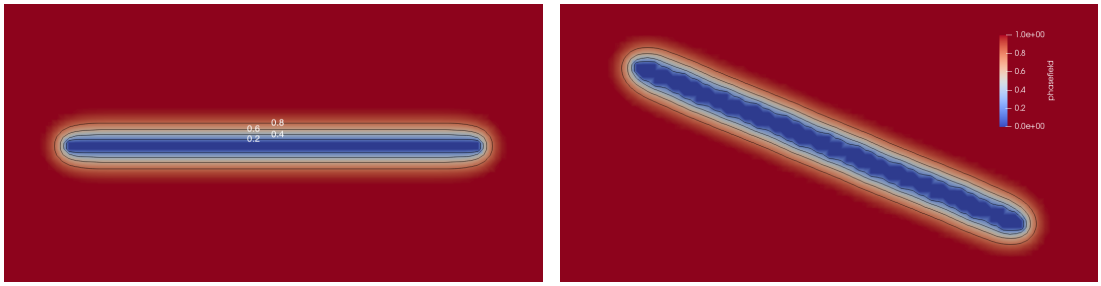

(a) Crack inclination of 0° (b) Crack inclination of 22.5°

Figure 8: Various level-sets drawn for $c_{LS} = 0.2$, 0.4, 0.6, and 0.8.

(element size) and Wheeler et al. [60] or Mikelić et al. [47] proposed to use the displacement value from the adjacent element. A linear level-set function proposed by Lee et al. [40] divides the domain Ω into "reservoir" Ω_R and "fracture" Ω_F as:

$$\varphi_{LS} > 0 \text{ for } x \in \Omega_R, \qquad \varphi_{LS} < 0 \text{ for } x \in \Omega_F, \qquad \varphi_{LS} = 0 \text{ for } x \in \Gamma_{LS}, \tag{20}$$

where the level-set function is defined as:

$$\varphi_{LS} = c_{LS} - v, \tag{21}$$

and c_{LS} is an arbitrary constant. Once the boundary between the fracture and the reservoir domain is delineated, the displacements in the normal direction to the level-set ($\vec{u}\cdot\vec{n}_{\Gamma_{LS}}$) are used to compute the crack opening. From any point on the crack, the normal vector to the level-set is drawn and $\vec{u}\cdot\vec{n}_{\Gamma_{LS}}$ is read at both intersections with the level-set (one forms a positive angle and the other negative) which are denoted by$(\vec{u}\cdot\vec{n}_{\Gamma_{LS}})^+$ and $(\vec{u}\cdot\vec{n}_{\Gamma_{LS}})^-$ respectively. Then the crack opening displacement is computed by summing the normal displacements from both sides as:[2]

$$w_{LS} := (\vec{u}\cdot\vec{n}_{\Gamma_{LS}})^+ + (\vec{u}\cdot\vec{n}_{\Gamma_{LS}})^-, \tag{22}$$

Fig. 8 shows the level-set lines drawn corresponding to different values of c_{LS}.

One of the open questions with (21) is to find the constant c_{LS}. In [40], it is suggested as 0.1, meaning that the crack normal displacement value corresponding to $v = 0.1$ is used as the displacement at the crack lip, but no specific justification for this suggested value was provided. In order to come up with an estimate for the constant, let us consider a 1D elastic rod ($x = [0, 1]$) with the Young's modulus of E. A crack is defined at $x = 0$ and the constant fluid pressure, p, is applied in the crack, which is regularised by the phase-field variable over the regularisation zone ($0 < x \leq 2\ell_s$). Thus the momentum balance reads as:

[2]The original model in [40] does not take the sum and instead multiplies $(\vec{u}\cdot\vec{n}_{\Gamma_{LS}})^+$ or $(\vec{u}\cdot\vec{n}_{\Gamma_{LS}})^-$by 2 which requires a symmetric $\vec{u}$ profile around the crack set Γ.

$$\begin{cases} \dfrac{d}{dx}\left(v^2\dfrac{du}{dx}\right) + p_D\dfrac{dv}{dx} = 0, & \text{for } 0 < x \leq 2\ell_s \\ \\ \dfrac{d}{dx}\left(\dfrac{du}{dx}\right) = 0, & \text{for } 2\ell_s < x \leq L \end{cases} \tag{23}$$

where $p_D = p/E$ and $\texttt{AT}_1$ v profile:

$$v = 1 - (1 - x/2\ell_s)^2, \tag{24}$$

is considered. With boundary conditions of $u = 0$ at $x = L$ and that u is continuous as $x = 2\ell_s$, we arrive at the following displacement field:

$$u = \begin{cases} p_D(2\ell_s - L) - 2p_D\ell_s^2\left(\dfrac{1}{x} + \dfrac{1}{x - 4\ell_s}\right), & \text{for } 0 < x \leq 2\ell_s \\ \\ p_D(x - L), & \text{for } 2\ell_s < x \leq L. \end{cases} \tag{25}$$

At the same time, we can solve the problem without the phase-field regularisation ($v = 1$, $\forall x \in [0, L]$) by applying the traction force explicitly at the boundary ($du/dx = p_D$ at $x = 0$). The displacement profile is then given as:

$$u = p_D(x - L). \tag{26}$$

Therefore, we can obtain the crack opening displacement, $u(0)$, as $-p_D L$. Then from (25), we can solve for the location x_{LS} where the displacement value is equivalent to the crack opening as:

$$x_{LS} = \ell_s(3 - \sqrt{5}). \tag{27}$$

Substituting (27) into (24), the corresponding phase-field value turns out to be:

$$v_{LS} = \frac{1 + \sqrt{5}}{2} - 1 \approx 0.618. \tag{28}$$

Computed crack openings from $c_{LS} = 0.618$ are compared with other c_{LS} for $a/h = 100$ and $\ell_s/h = 2$ in Figs 9. The errors are computed simply as a difference from the closed form solution. For a crack with the inclination of 0° from the horizontal axis, though all the cases of c_{LS} produce reasonable crack opening displacement profiles, $c_{LS} = 0.618$ results in a good overall estimate[3]. Perhaps more prominent observation can be made from a crack with the inclination of 22.5° in which the crack is not aligned with the underlining structural grid. Small values of c_{LS} (e.g. $c_{LS} = 0.1$ or 0.3) produce very corrugated profiles of the crack openings. This is because the distance from the crack for small values of c_{LS} is more impacted by the grid as can be seen in the level-sets in Fig. 8(b). Although this impact was not particularly considered in arriving at the optimal c_{LS} value, it shows that small c_{LS} values are not favourable when cracks are not aligned with the grid. Based on the analyses, $c_{LS} = 0.618$ is used for all the subsequent analyses. The detailed procedures for crack opening computation are described in Algorithm 2.

[3]As the number is derived from the 1D analysis, the argument for $c_{LS} = 0.618$ will not hold if a problem deviates from the 1D setting (e.g. near crack tip). However, throughout the examples in this study $c_{LS} = 0.618$ generates a consistently good estimate.

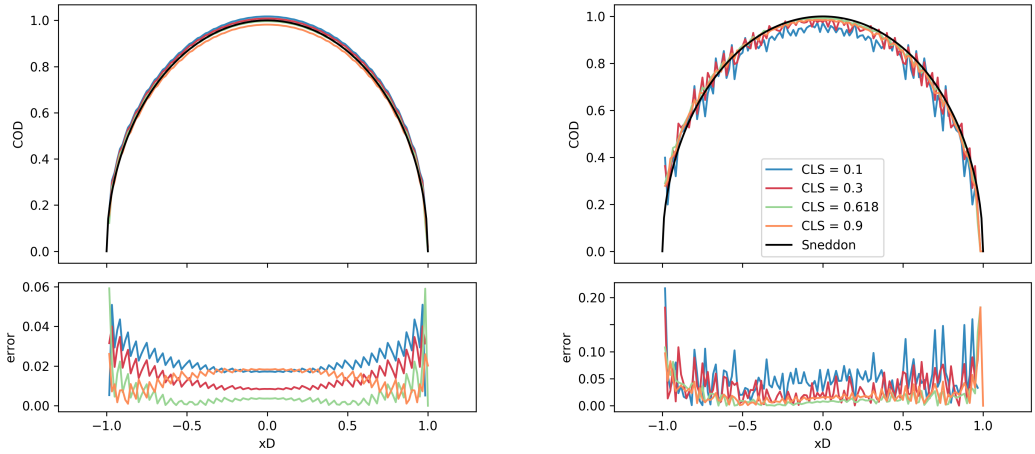

(a) Crack inclination of 0°

(b) Crack inclination of 22.5°

Figure 9: Comparison of crack opening profiles for $c_{LS} = 0.1$, 0.3, 0.618, and 0.9 to the closed form solution and the errors.

Algorithm 2 Level-set width finding algorithm

1: Compute piecewise linear contour of the phase-field for a given level-set value using the vtkContourFilter.
2: **for all** straight line segments c_i with endpoints $\mathbf{x}_i$ and $\mathbf{x}_{i+1}$: **do**
3: $\quad \vec{n}_i = \mathcal{R}(\mathbf{x}_{i+1} - \mathbf{x}_i)/|\mathbf{x}_{i+1} - \mathbf{x}_i|$ // Normal vector of c_i
4: // where $\mathcal{R} := \begin{bmatrix} 0 & -1 \\ 1 & 0 \end{bmatrix}$
5: $\quad \vec{u}_i = \vec{u}(\mathbf{x}_i) + \vec{u}(\mathbf{x}_{i+1})$ // Sum of the displacements on c_i
6: $\quad w_i = \vec{u}_i \cdot \vec{n}_i$ // Width on c_i

4. Results and discussions

In this section, we compare the two approaches described in the previous section under various conditions using structured quadrilateral elements. Specifically, we study the behaviours from the two approaches with different mesh resolutions and crack inclinations against the structured quadrilateral mesh. Additionally, we test the methods with non-uniform displacement fields and investigate the impacts of the regularisation length.

4.1. Mesh resolution and crack inclination to the mesh

First we test the methods with a crack inclination of 0° from the x-axis as shown in Fig. 10(e) with four different mesh resolutions ($a/h = 10$, $a/h = 17$, $a/h = 33$, and $a/h = 100$). The ratio of the mesh resolution to the regularisation length is kept constant ($\ell_s/h = 3$) unless otherwise stated. Fig. 10 shows computed results using both the line integral and the level-set methods from the four different mesh resolutions compared against the closed form solution [56]. For $a/h = 10$ and $a/h = 17$, the computed results are slightly underestimated and more so for the level-set method while both approaches with the resolution of $a/h = 33$ reproduced fairly reasonable crack opening displacements except near the crack tips. With the resolution of $a/h = 100$, the crack aperture was recovered accurately even near the crack tips.

A scenario where cracks are aligned with the computation grid is a benign case for computation but in practice, we will not always find ourselves in such a fortunate situation for complex fracture propagation. Thus in the following examples, we examine the two computation approaches under two different crack inclinations of 22.5° and 45° from the horizontal axis respectively in various mesh resolution.

Fig. 11 shows computation results from the 22.5° inclination which turned out to be the most challenging in generating a smooth crack opening profile. This is because how the properties are interpolated within an element in the current approaches for the line integral method as it suffers from oscillations in the evaluated distance to the crack along the normal direction. Although this effect can be alleviated by refining the mesh to some extent, a certain level of non-smoothness was observed in all the resolution cases carried out in this study. On the other hand, the level-set method is able to produce a smooth profile as discussed in the previous section. The opening profile near the crack tip itself improved with mesh refinement.

Simulation results with 45° inclination are shown in Fig. 12. They do not exhibit non-smooth opening profiles like the cases with 22.5° inclination for the line integral method. Instead, some asymmetric bias can be seen in the low resolution case (Fig. 12(a)). As the 45° line crack is discretised with structured elements, there is always one node more (or one node less) at the crack tip either in x- or y-direction representing the crack ($v = 0$), which causes a slight bias to either side of the crack in computation. However, this issue gets quickly resolved with mesh refinement and in the high-resolution cases (Figs. 12(c) and 12(d)), the profiles were indeed computed as good as the aligned mesh cases including near the crack tips.

4.2. Under external loading

A symmetric displacement profile around the crack Γ may hardly be the case in realistic hydraulic fracturing situations because of the presence of other cracks, or in-situ stresses in the earth crust. For this reason, scenarios with boundary loading are examined in this subsection. A deformed displacement profile was induced simply by applying prescribed displacements on the boundaries as shown in Fig. 13(d). Note that because of the asymmetric displacement field, $(\vec{u} \cdot \vec{n}_{\Gamma_{LS}})^+$ is not

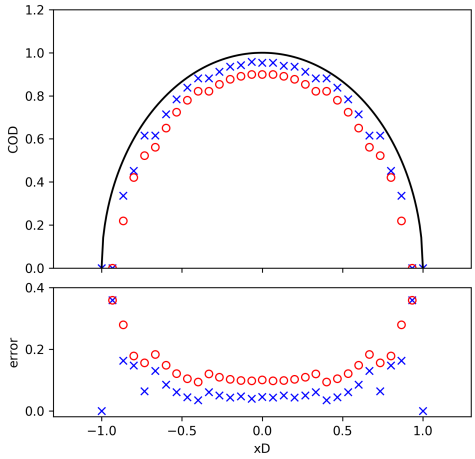

(a) $a/h = 10$

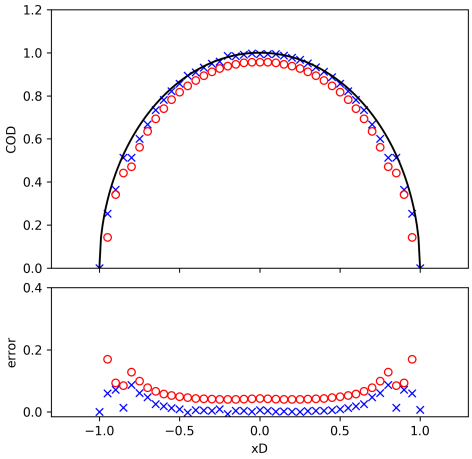

(b) $a/h = 17$

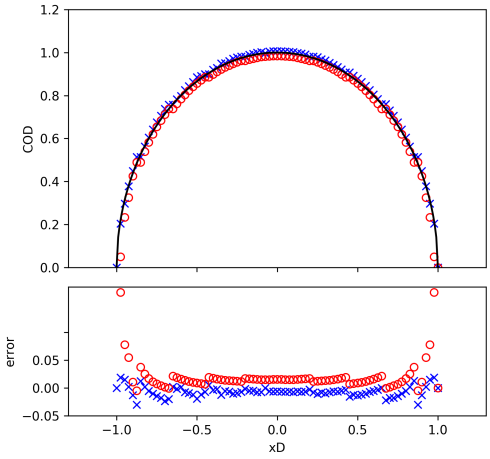

(c) $a/h = 33$

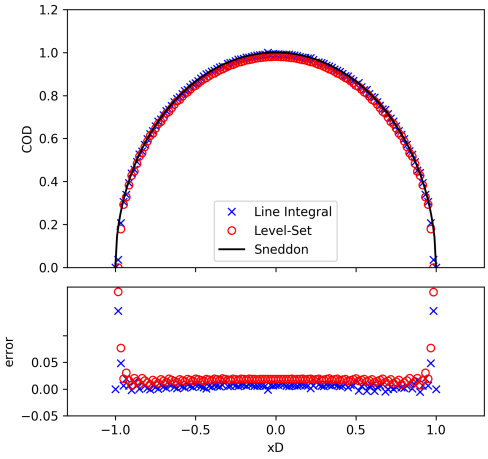

(d) $a/h = 100$

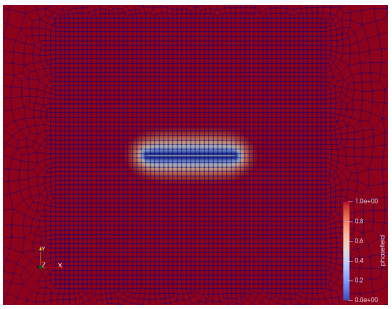

(e) The profile of the crack

Figure 10: Crack opening profiles with different mesh resolution for a horizontal crack (0° from the horizontal axis) and the errors compared from the closed form solution.

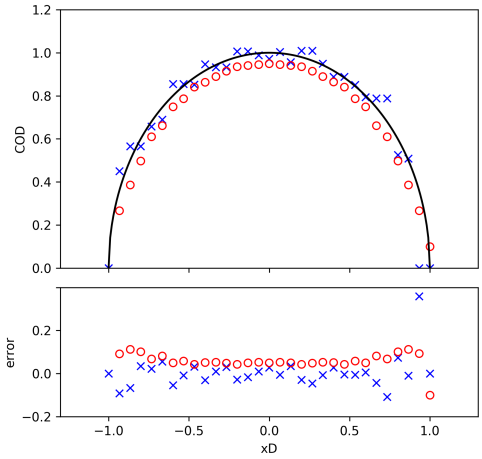

(a) $a/h = 10$

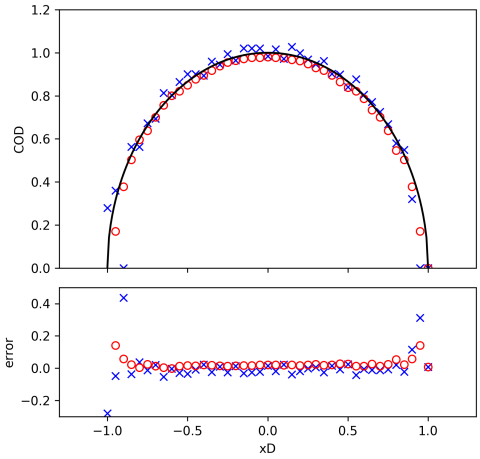

(b) $a/h = 17$

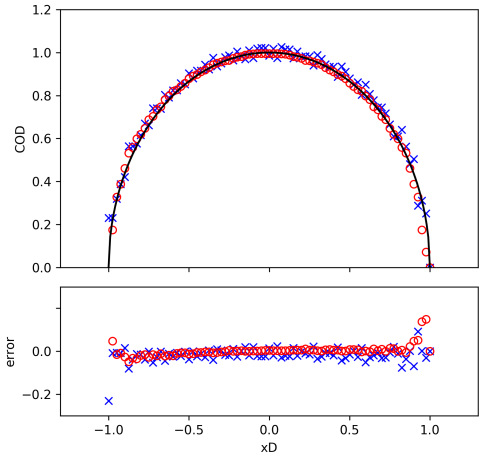

(c) $a/h = 33$

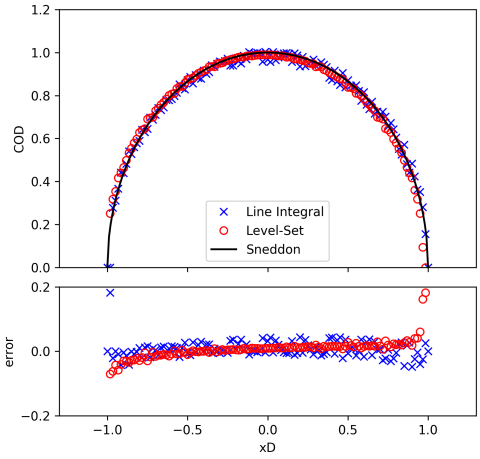

(d) $a/h = 100$

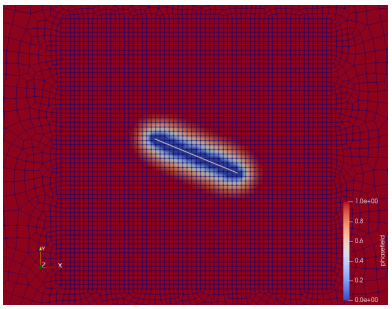

(e) The profile of the crack

Figure 11: Crack opening profiles with different mesh resolution for a horizontal crack (22.5° from the horizontal axis) and the errors compared from the closed form solution.

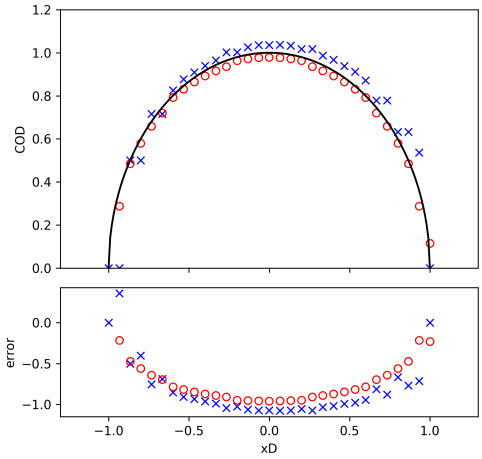

(a) $a/h = 10$

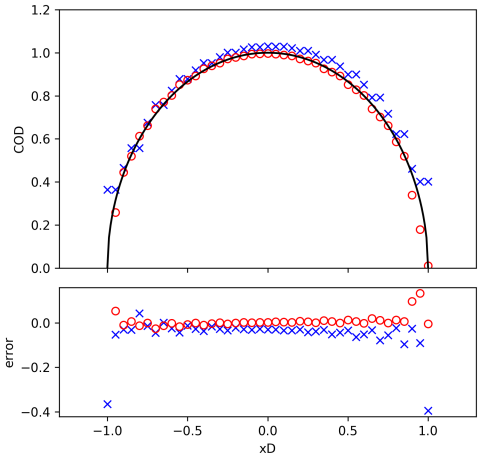

(b) $a/h = 17$

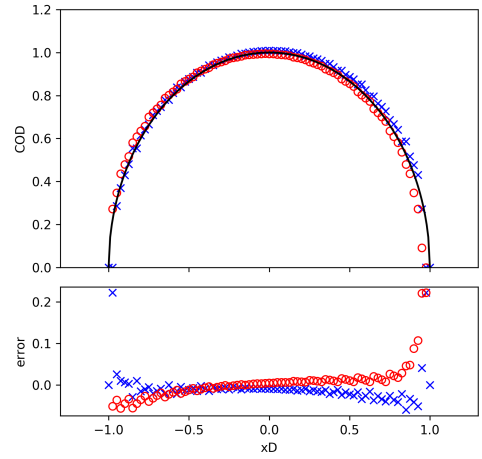

(c) $a/h = 33$

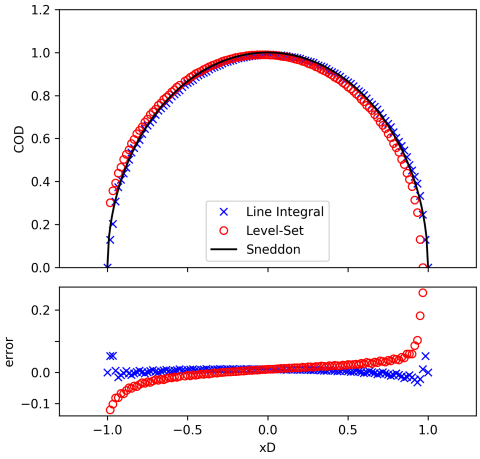

(d) $a/h = 100$

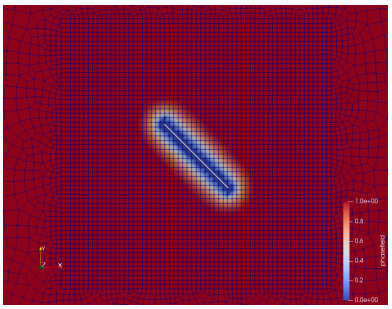

(e) The profile of the crack

Figure 12: Crack opening profiles with different mesh resolution for a horizontal crack (45° from the horizontal axis) and the errors compared from the closed form solution.

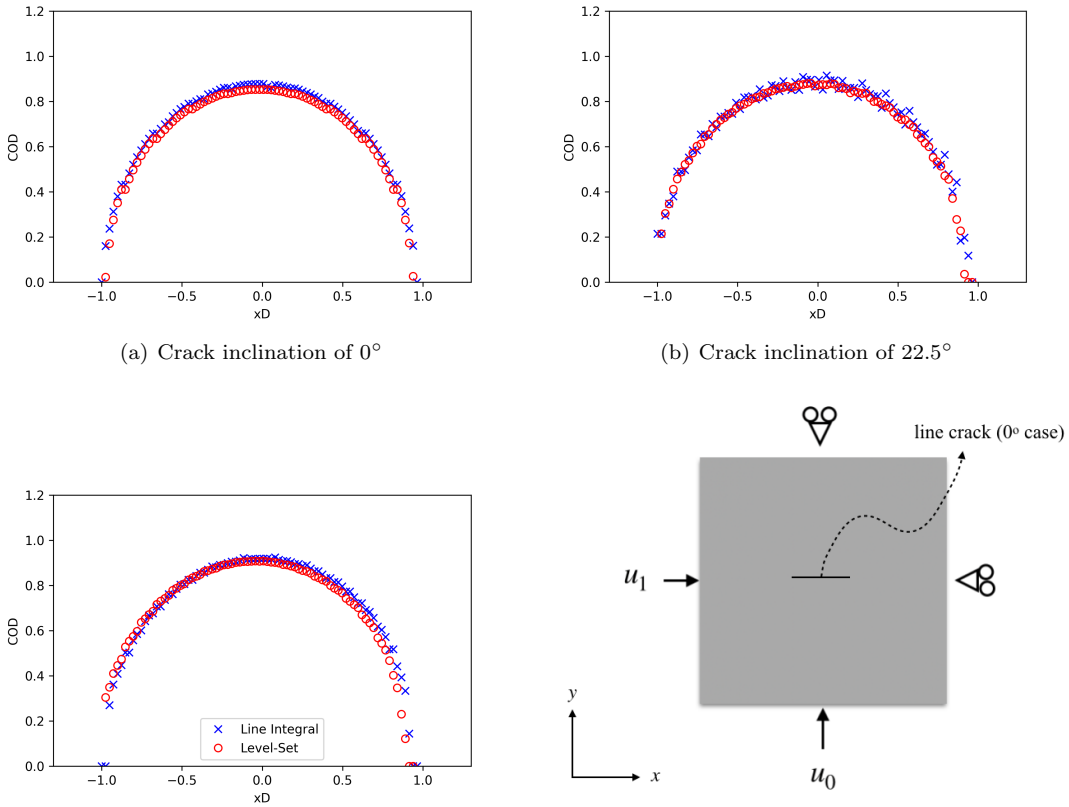

(a) Crack inclination of 0°

(b) Crack inclination of 22.5°

(c) Crack inclination of 45°

(d) Schematic of loaded domain

Figure 13: Crack opening profiles under loadings.

identical to $(\vec{u} \cdot \vec{n}_{\Gamma_{LS}})^-$. Thus they need to be summed to cancel out the background displacement field rather than multiplying $(\vec{u} \cdot \vec{n}_{\Gamma_{LS}})^+$ or $(\vec{u} \cdot \vec{n}_{\Gamma_{LS}})^-$ by two as proposed in [40]. Computed crack opening profiles with different inclinations and the mesh resolution of $a/h = 33$ are shown in Fig. 13. Since no closed form solution is available, they were only cross-verified between the two methods.

We can observe similarly to the previous cases that the inclination with 22.5° has a non-smooth profile for the line integral method but apart from this both approaches agree very well in all the inclinations.

4.3. Various regularisation length

We study the impacts of the regularisation length ℓ_s in this subsection. In all the previous examples, the regularisation length was kept at a constant relative to the element size ($\ell_s/h = 3$). Fig. 14 compares the results from various regularisation lengths ($\ell_s/h = 1.5$, $\ell_s/h = 2$, $\ell_s/h = 4$, and $\ell_s/h = 5$) while keeping the mesh resolution constant at $a/h = 33$ with the crack inclination of 0°. Firstly, as suggested by (28), the threshold value is not a function of the regularisation length

but a constant, and we can confirm that all the cases show nearly identical profiles computed from either approach. Secondly, as the regularisation length increases, the crack presentation becomes more diffused and obviously, it harms the reproduction of the crack opening profile especially near the crack tip. From these computations, we can see that the regularisation length greater than $3h$ would not resolve the crack opening profile well in $\texttt{AT}_1$ and it should be considered as an upper limit especially if crack opening resolution is of importance.

4.4. Critically loaded and propagating crack

Though minimisation of (4) is achieved in a quasi-static manner without a notion of "static" or "propagating" except for an irreversible crack growth constraint[4], the phase-field evolution will start from the beginning of loading with a model such as $\texttt{AT}_2$. Even with a model employed in this study, $\texttt{AT}_1$, which is equipped with the elastic limit [50], the phase-field is known to show an "add-crack" effect near the critical loading [57]. To test the feasibility of the approaches under such critical loading, we compare crack openings with the closed form solution using a classical hydraulic fracture propagation problem in the toughness dominated regime without leak-off to the formation based on Sneddon-Lowengrub solution [11, 25, 26, 37]. Considering an infinite 2D domain with a line $[-a_0, a_0] \times \{0\}$ similar to Fig. 2, the critical volume for crack propagation is $V_c := \sqrt{\dfrac{4\pi G_c a_0^3}{E'ec}}$. The pressure and the crack length evolutions can be obtained as:

$$p(V) = \begin{cases} \dfrac{E'V}{2\pi a_0^2} & V < V_c \\ \left[\dfrac{2E'G_c^2}{\pi V}\right]^{\frac{1}{3}} & V \geq V_c, \end{cases} \tag{29}$$

and

$$a(V) = \begin{cases} a_0 < V_c \\ \left[\dfrac{2E'V^2}{4\pi G_c}\right]^{\frac{1}{3}} & V \geq V_c, \end{cases} \tag{30}$$

Since the toughness dominated regime considers no pressure drop within the crack, the numerical solution for pressure does not require the crack opening profile. The mass balance instead is ensured as a constrain at each discrete time step by equating the injected fluid volume to the crack volume as $V = \int_\Omega u \cdot \nabla v \, \mathrm{d}\Omega$. We refer the numerical implementation details to [11, 64] and compare the pressure and length evolutions in Fig. 15. The measure of the crack length is calculated by dividing the regularised surface energy term computed in (4), $\dfrac{G_c}{4c_n} \int_\Omega \left(\frac{(1-v)^n}{\ell_s} + \ell_s |\nabla v|^2 \right) \mathrm{d}V$, by G_c. To emphasize the crack evolution, the results in this section are presented without normalising by the maximum value.

As highlighted in red in Fig. 15, we picked three time steps to verify the crack openings, which are 1) a "pre-propagation" ($V = 0.06$), 2) immediately prior to propagation ($V = 0.13$), and 3) "post-propagation" ($V = 0.16$). The crack opening displacements from the line integral and level-set methods are compared against the closed form solution in Fig. 16 and the corresponding phase-field

[4]Several approaches to take into account of the irreversibility exist (see [5]). In this example, we provide it as a constraint as $v^{k-1} \subset v^k$ with k denoting the time step.

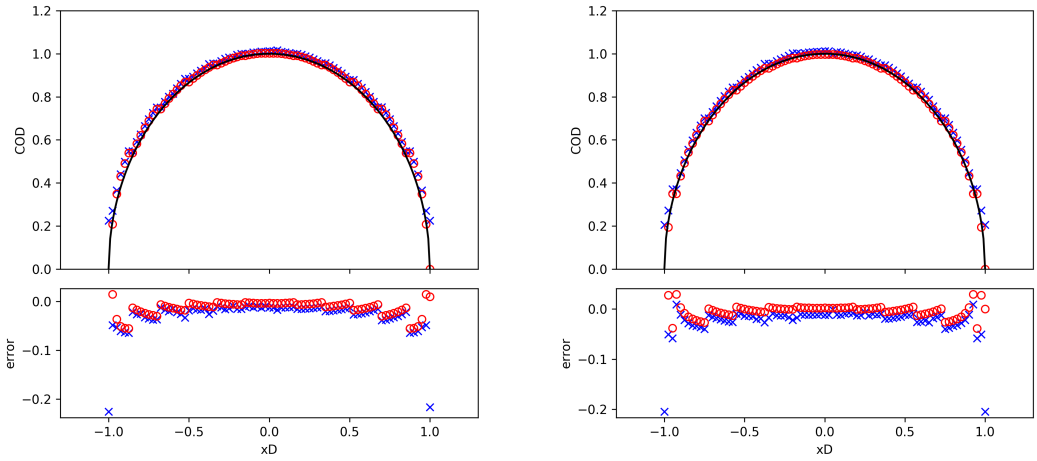

(a) $\ell_s/h = 1.5$

(b) $\ell_s/h = 2$

(c) $\ell_s/h = 4$

(d) $\ell_s/h = 5$

Figure 14: Crack opening profiles with various regularisation length and the errors compared to the closed form solution.

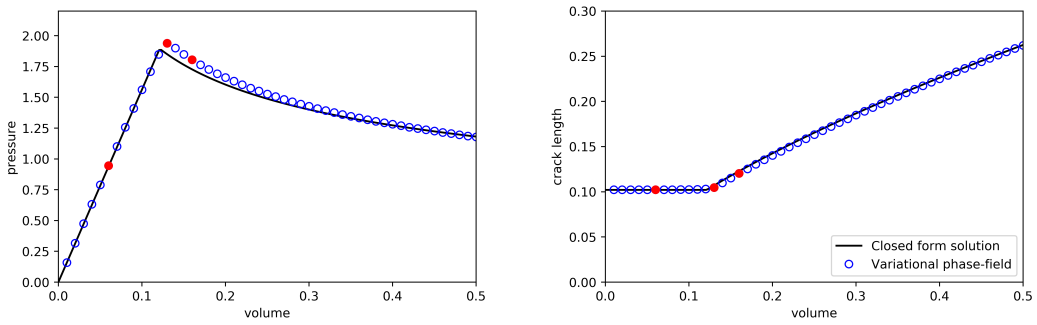

(a) Pressure vs. injected volume.

(b) Length vs. injected volume

Figure 15: Comparison of the hydraulic fracture propagation problem between the closed form solution and the variational phase-field model. The red circles indicate the steps where the crack opening displacements are compared.

profiles near the crack tip in Fig. 17. The numerically computed crack length from the phase-field profile remains almost the same until the propagation but grows slightly from $a(0.06) = 0.1023$ to $a(0.13) = 0.1047$, which can be observed in Fig. 17(b) as increase in the surface energy. Also, as the crack size is slightly overestimated at the critically loaded step, so are the crack openings by both approaches (Fig. 16(b)) compared to the pre-propagation step (Fig. 16(a)). Even though the phase-field profile evolves before the propagation to its optimal profile for the theoretical critical energy release rate [57], the evolution is confined around the crack tip and its impacts on the crack opening profile is fairly limited. Besides this observation, both the approaches compute the crack opening growth quite accurately at all the steps.

5. Conclusions

Despite increasing attention to phase-field models for fracture, resolution of crack opening displacement has not been carefully investigated for justifiable reasons. However, since quantitative identification of crack opening is crucial in certain applications (e.g. hydraulic fracturing), this study focused on the quantitative verification of the two most commonly used approaches under different scenarios that can be encountered in realistic simulations. Although the approximation with the line integral can be shown to be theoretically robust (2.2), its actual implementation requires some adaptations in crack normal computation and special treatment near the crack tips. Thus, we have proposed a practically tractable line integral algorithm and verified it under various different scenarios.

The other proposed method, which is based on the level-set function, lacked a robust justification for the ad-hoc parameter required in the function. We proposed a value for the parameter to define the level-set from the 1D elastic rod analysis and verified it under various situations together with the line integral approach. The constant value proposed, $c_{LS} = (1+\sqrt{5})/2-1$, was tested reasonably well for all the cases considered in this study.

Also, the impacts of regularisation length on the crack opening displacement were assessed. Based on the computations, the regularisation length greater than $3h$ appeared to be non-desirable for crack opening computation.

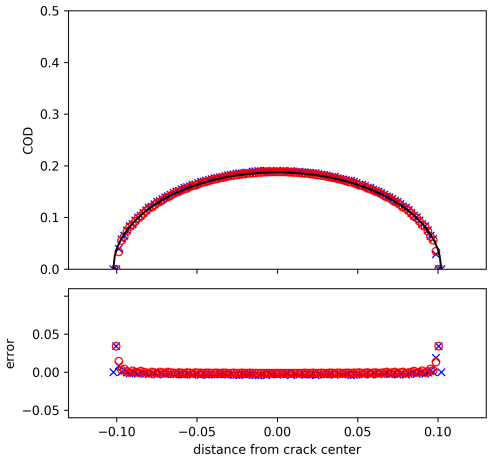

(a) Pre-propagation at $V = 0.06$.

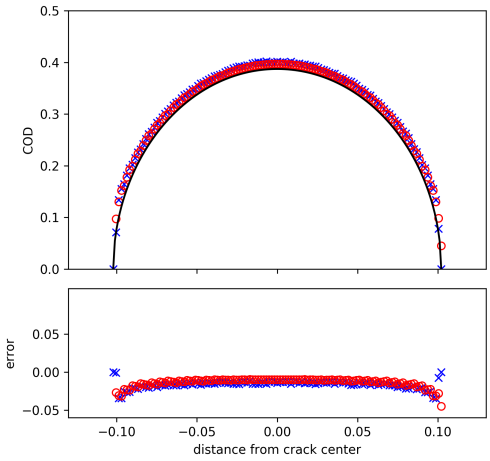

(b) Critical point at $V = 0.13$.

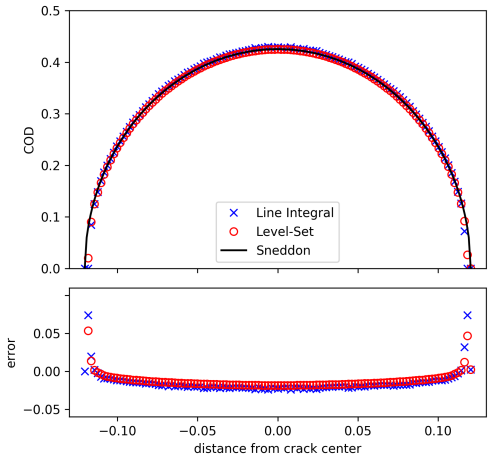

(c) Post-propagation at $V = 0.16$.

Figure 16: Comparison of the hydraulic fracture propagation problem between the closed form solution and the variational phase-field model. The red circles indicate the steps where the crack opening displacements are compared.

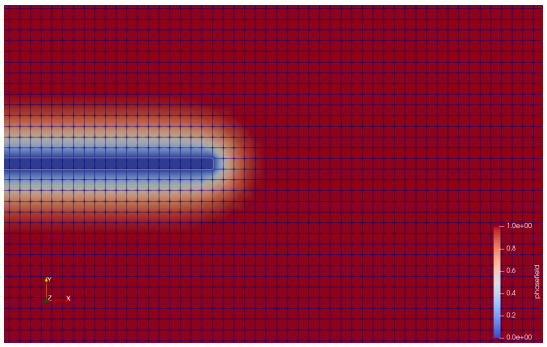

(a) Phase-field profile at $V = 0.06$.

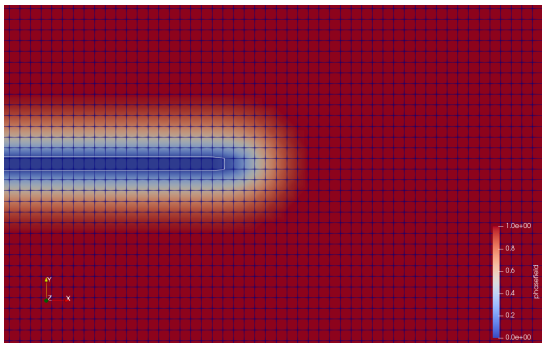

(b) Phase-field profile at $V = 0.13$.

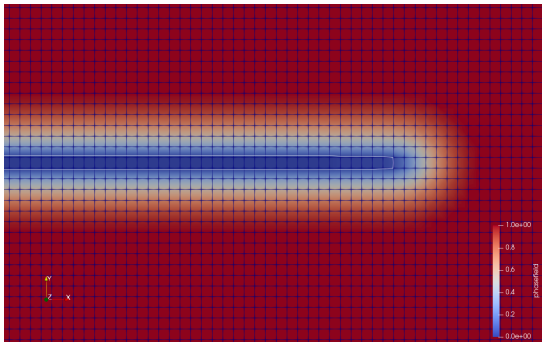

(c) Phase-field profile at $V = 0.16$.

Figure 17: Phase-field profiles at the pre-propagation step ($V = 0.06$) and the step immediately prior to propagation $V = 0.13$. The contours of the phase-field variable = 0.05 are drawn to indicate the crack tips.

Finally, the approaches presented were tested under critically loaded and propagating crack. Despite the slight evolution of the phase-field profile at the critical load and post-propagation, both approaches were able to compute the crack openings accurately.

6. Author Contributions

Keita Yoshioka: Conceptualization, Methodology, Software, Validation, Formal Analysis, Writing - Original Draft, Visualization. **Dmitri Naumov:** Methodology, Software, Writing - Review & Editing, Visualization. **Olaf Koldizt:** Writing - Review & Editing, Project administration, Funding acquisition.

7. Acknowledgements

The authors gratefully acknowledge the following grants:the German Federal Ministry of Education and Research (BMBF) for the GeomInt project (Grant Number 03G0866A, within the BMBF Geoscientific Research Program "Geo:N Geosciences for Sustainability"), EURAD - the European Joint Programme on Radioactive Waste Management for DONUT (Grant Agreement No 847593), and BMBF and Helmholtz Association for iCROSS project (grant numbers 02NUK053E and SO-093). KY thanks Renchao Lu for his help with the artworks in the manuscript. Finally, the authors are grateful for the reviews provided by anonymous reviewers.

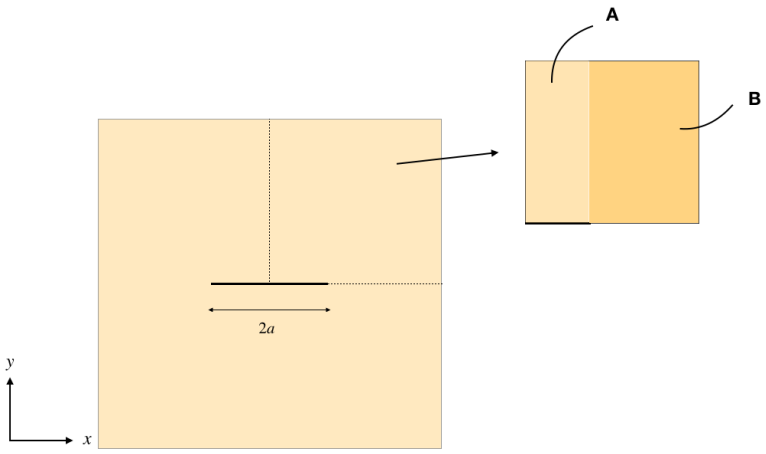

Figure 18: Decomposition of the surface integral into region A and B for the surface energy estimates.

8. Appendix

In this Appendix, we show how the effective toughness and crack length for a 2D line crack are computed as shown in Fig. 2. The surface energy is regularised by the phase-field variable v and is given as $\int_S S(x, v, v')\,\mathrm{d}S$ and as in Fig. 18, the integral can be divided into two parts:

$$\begin{aligned}\frac{1}{4}G_c(2a) &= \frac{1}{4}\int_S S(x,v,v')\mathrm{d}S \\ &= \int_{S_A} S(x,v,v')\mathrm{d}S + \int_{S_B} S(x,v,v')\mathrm{d}S. \end{aligned} \tag{31}$$

8.1. $\mathtt{AT}_1$ case

In the region A in Fig. 18, the profiles of v and v' for $\mathtt{AT}_1$ are approximated as a function of y only as:

$$v(y) = \begin{cases} 0 & y < \dfrac{h}{2} \\ 1 - \left(1 - \dfrac{y - h/2}{2\ell_s}\right)^2 & \dfrac{h}{2} \le y < 2\ell_s + \dfrac{h}{2} \\ 1 & 2\ell_s + \dfrac{h}{2} \le y, \end{cases} \tag{32}$$

and

$$v'(y) = \begin{cases} 0 & y < \dfrac{h}{2} \\ \dfrac{1}{\ell_s}\left(1 - \dfrac{y - h/2}{2\ell_s}\right) & \dfrac{h}{2} \le y < 2\ell_s + \dfrac{h}{2} \\ 0 & 2\ell_s + \dfrac{h}{2} \le y. \end{cases} \tag{33}$$

Now the surface energy in region A is given by

$$\int_{S_A} S(x,v,v')\mathrm{d}S = \frac{3}{8}G_c \int_0^{\infty}\int_0^{a}\left(\frac{1-v}{\ell_s} + (v')^2\right)\mathrm{d}x\mathrm{d}y. \tag{34}$$

Substituting (32) and (33) into (34) gives

$$\begin{aligned}\int_{S_A} S(x,v,v')\mathrm{d}S &= \frac{3}{8}G_c a\left\{\int_0^{\frac{h}{2}}\frac{1}{\ell_s}\mathrm{d}y + \int_{\frac{h}{2}}^{2\ell_s+\frac{h}{2}}\frac{2}{\ell_s}\left(1-\frac{y-h/2}{2\ell_s}\right)^2\mathrm{d}y\right\}\\ &= \frac{3}{8}G_c a\left(\frac{h}{2\ell_s}+\frac{4}{3}\right).\end{aligned} \tag{35}$$

In the region B, the optimal profiles are approximated as:

$$v(r) = \begin{cases} 1-\left(1-\dfrac{r}{2\ell_s}\right)^2 & r < 2\ell_s \\ 1 & r \geq 2\ell_s, \end{cases} \tag{36}$$

and

$$v'(r) = \begin{cases} -\dfrac{1}{\ell_s}\left(1-\dfrac{r}{2\ell_s}\right) & r < 2\ell_s \\ 0 & r \geq 2\ell_s \end{cases} \tag{37}$$

where r is the distance from the crack tip, $r = \sqrt{(x-a/2)^2+y^2}$. Then the integral over the region B is

$$\begin{aligned}\int_{S_B} S(x,v,v')\mathrm{d}S &= \frac{3}{8}G_c\int_0^{\infty}\int_0^{\frac{\pi}{2}}\left(\frac{1-v}{\ell_s} + \ell_s\left|\nabla v\right|^2\right)r\mathrm{d}r\mathrm{d}\theta\\ &= \frac{\pi}{8}\ell_s G_c.\end{aligned} \tag{38}$$

Thus the surface energy can be equated as

$$\begin{aligned}\frac{1}{4}G_c^{\mathrm{eff}}(2a^{\mathrm{eff}}) &= \int_{S_A} S(x,v,v')\mathrm{d}S + \int_{S_B} S(x,v,v')\mathrm{d}S\\ &= \frac{3}{8}G_c a\left(\frac{h}{2\ell_s}+\frac{3}{4}\right) + \frac{\pi}{8}\ell_s G_c\end{aligned} \tag{39}$$

Rearranging yields

$$G_c^{\mathrm{eff}}a^{\mathrm{eff}} = G_c\left(\frac{3h}{8\ell_s}+1\right)a\left(1+\frac{\pi\ell_s/4}{a(3h/8\ell_s+1)}\right). \tag{40}$$

Therefore, in the regularised profile, we can consider the effective fracture toughness and length as in (16) and (17) respectively.

8.2. $\mathtt{AT}_2$ case

In the region A, the profiles of v and v' for $\mathtt{AT}_2$ are approximated with:

$$v(y) = \begin{cases} 0 & y < \dfrac{h}{2} \\ 1 - \exp\left(-\dfrac{y - h/2}{\ell_s}\right) & \dfrac{h}{2} \leq y \end{cases} \tag{41}$$

$$v'(y) = \begin{cases} 0 & y < \dfrac{h}{2} \\ -\dfrac{1}{\ell_s}\exp\left(-\dfrac{y - h/2}{\ell_s}\right) & \dfrac{h}{2} \leq y \end{cases} \tag{42}$$

The surface energy in the region A can be similarly computed as

$$\int_{S_A} S(x, d, d')\mathrm{d}S = G_c a_0 \left(\frac{h}{4\ell_s} + \frac{1}{2}\right). \tag{43}$$

In the region B, the optimal damage profile is similarly approximated as:

$$v = 1 - \exp\left(-\frac{r}{\ell_s}\right) \tag{44}$$

The surface energy in the region B is then calculated as

$$\begin{aligned} \int_{S_B} S(x, v, v')\mathrm{d}S &= \frac{G_c}{2}\int_0^{\infty}\int_0^{\frac{\pi}{2}} \left(\frac{(1-v)^2}{\ell_s} + \ell_s \left|\nabla v\right|^2\right) r\mathrm{d}r\mathrm{d}\theta \\ &= \frac{\pi}{8}\ell_s G_c. \end{aligned} \tag{45}$$

By equating the energies, we have

$$G_c^{\mathrm{eff}} a^{\mathrm{eff}} = G_c \left(\frac{h}{2\ell_s} + 1\right) a \left(1 + \frac{\pi\ell_s/4}{a(h/2\ell_s + 1)}\right). \tag{46}$$

Again, the regularised effective fracture toughness and length can be regarded as in (16) and (18) respectively.

[1] J. Adachi, E. Siebrits, A. Peirce, and J. Desroches. Computer simulation of hydraulic fractures. *International Journal of Rock Mechanics and Mining Sciences*, 44(5):739–757, 2007.

[2] R. Alessi, J. J. Marigo, C. Maurini, and S. Vidoli. Coupling damage and plasticity for a phase-field regularisation of brittle, cohesive and ductile fracture: One-dimensional examples. *International Journal of Mechanical Sciences*, pages 1–18, 2017.

[3] R. Alessi, S. Vidoli, and L. De Lorenzis. A phenomenological approach to fatigue with a variational phase-field model: The one-dimensional case. *Engineering Fracture Mechanics*, 190:53–73, 2018.

[4] M. Ambati, T. Gerasimov, and L. De Lorenzis. Phase-field modeling of ductile fracture. *Computational Mechanics*, 55(5):1017–1040, 2015.

[5] Marreddy Ambati, Tymofiy Gerasimov, and Laura De Lorenzis. A review on phase-field models of brittle fracture and a new fast hybrid formulation. *Computational Mechanics*, 55(2):383–405, 2014.

[6] H. Amor, J.-J. Marigo, and C. Maurini. Regularized formulation of the variational brittle fracture with unilateral contact: Numerical experiments. *Journal of the Mechanics and Physics of Solids*, 57(8):1209 – 1229, 2009.

[7] S. Balay, S. Abhyankar, M. F. Adams, J. Brown, P. Brune, K. Buschelman, L Dalcin, A. Dener, V. Eijkhout, W. D. Gropp, D. Karpeyev, D. Kaushik, M. G. Knepley, D. A. May, L. C. McInnes, R. T. Mills, T. Munson, K. Rupp, P. Sanan, B. F. Smith, S. Zampini, H. Zhang, and H. Zhang. PETSc users manual. Technical Report ANL-95/11 - Revision 3.11, Argonne National Laboratory, 2019.

[8] S. Balay, S. Abhyankar, M. F. Adams, J. Brown, P. Brune, K. Buschelman, L Dalcin, A. Dener, V. Eijkhout, W. D. Gropp, D. Karpeyev, D. Kaushik, M. G. Knepley, D. A. May, L. C. McInnes, R. T. Mills, T. Munson, K. Rupp, P. Sanan, B. F. Smith, S. Zampini, H. Zhang, and H. Zhang. PETSc Web page, 2019.

[9] M.A. Biot. General theory of three-dimensional consolidation. *Journal of Applied Physics*, 12(2):155–164, 1941.

[10] M.J. Borden, C.V. Verhoosel, M.A. Scott, T.J.R. Hughes, and C.M. Landis. A phase-field description of dynamic brittle fracture. *Computer Methods in Applied Mechanics and Engineering*, 217-220:77–95, 2012.

[11] B. Bourdin, C. Chukwudozie, and K. Yoshioka. A variational approach to the numerical simulation of hydraulic fracturing. In *SPE ATCE 2012*, 2012.

[12] B. Bourdin, G.A. Francfort, and J.-J. Marigo. Numerical experiments in revisited brittle fracture. *J. Mech. and Phys. of Solids*, 48(4):797–826, 2000.

[13] B. Bourdin, G.A. Francfort, and J.-J. Marigo. The variational approach to fracture. *Journal of Elasticity*, 91(1-3):5–148, 2008.

[14] B. Bourdin, C.J. Larsen, and C.L. Richardson. A time-discrete model for dynamic fracture based on crack regularization. *International Journal of Fracture*, 168(2):133–143, 2011.

[15] A. Braides. *Approximation of Free-Discontinuity Problems*. Number 1694 in Lecture Notes in Mathematics. Springer, 1998.

[16] T. Cajuhi, L. Sanavia, and Laura De Lorenzis. Phase-field modeling of fracture in variably saturated porous media. *Computational Mechanics*, pages 1–20, 2017.

[17] J. Choo and W.C. Sun. Cracking and damage from crystallization in pores: Coupled chemo-hydro-mechanics and phase-field modeling. *Computer Methods in Applied Mechanics and Engineering*, 335(March):347–379, 2018.

[18] C. Chukwudozie, B. Bourdin, and K. Yoshioka. A variational phase-field model for hydraulic fracturing in porous media. *Computer Methods in Applied Mechanics and Engineering*, 347:957–982, 2019.

[19] R. de Borst. Chapter 7 - phase-field methods for fracture. In R. de Borst, editor, *Computational Methods for Fracture in Porous Media*, pages 155 – 184. Elsevier, 2018.

[20] E. Detournay. Mechanics of hydraulic fractures. *Annual Review of Fluid Mechanics*, 48:311–339, 2016.

[21] W. Ehlers and C. Luo. A phase-field approach embedded in the Theory of Porous Media for the description of dynamic hydraulic fracturing. *Computer Methods in Applied Mechanics and Engineering*, 315:348–368, 2017.

[22] P. Farrell and C. Maurini. Linear and nonlinear solvers for variational phase-field models of brittle fracture. *International Journal for Numerical Methods in Engineering*, 109(5):648–667, 2017.

[23] G.A. Francfort and J.-J Marigo. Revisiting brittle fracture as an energy minimization problem. *J. Mech. and Phys. of Solids*, 46(8):1319–1342, 1998.

[24] T. Gerasimov and L. De Lorenzis. A line search assisted monolithic approach for phase-field computing of brittle fracture. *Computer Methods in Applied Mechanics and Engineering*, 312:276 – 303, 2016. Phase Field Approaches to Fracture.

[25] T Gerasimov and L De Lorenzis. On penalization in variational phase-field models of brittle fracture. *Computer Methods in Applied Mechanics and Engineering*, 354:990–1026, 2019.

[26] P. Gupta and C. A. Duarte. Particle Shape Effect on Macro-and Micro Behaviours of Monodisperse Ellipsoids. *International Journal for Numerical and Analytical Methods in Geomechanics*, 38:1397–1430, 2014.

[27] V. Hakim and A. Karma. Laws of crack motion and phase-field models of fracture. *Journal of the Mechanics and Physics of Solids*, 57(2):342–368, 2009.

[28] Y. Heider and B. Markert. A phase-field modeling approach of hydraulic fracture in saturated porous media. *Mechanics Research Communications*, 80:38–46, 2017.

[29] T. Heister, M.F. Wheeler, and T. Wick. A primal-dual active set method and predictor-corrector mesh adaptivity for computing fracture propagation using a phase-field approach. *Computer Methods in Applied Mechanics and Engineering*, 290:466–495, 2015.

[30] M. Hofacker and C. Miehe. Continuum phase field modeling of dynamic fracture: Variational principles and staggered FE implementation. *International Journal of Fracture*, 178(1-2):113–129, 2012.

[31] Markus Klinsmann, Daniele Rosato, Marc Kamlah, and Robert M. McMeeking. An assessment of the phase field formulation for crack growth. *Computer Methods in Applied Mechanics and Engineering*, 294:313–330, 2015.

[32] O. Kolditz, S. Bauer, L. Bilke, N. Böttcher, J.O. Delfs, T. Fischer, U.J. Görke, T. Kalbacher, G. Kosakowski, C.I. McDermott, et al. OpenGeoSys: an open-source initiative for numerical simulation of thermo-hydro-mechanical/chemical (THM/C) processes in porous media. *Environmental Earth Sciences*, 67(2):589–599, 2012.

[33] O. Kolditz, T. Nagel, H. Shao, W. Wang, and S. Bauer. *Thermo-Hydro-Mechanical-Chemical Processes in Fractured Porous Media: Modelling and Benchmarking*. Springer, 2017.

[34] C. Kuhn and R. Müller. A continuum phase field model for fracture. *Engineering Fracture Mechanics*, 77(18):3625–3634, 2010.

[35] C. Kuhn, T. Noll, and R. Müller. On phase field modeling of ductile fracture. *GAMM Mitteilungen*, 39(1):35–54, 2016.

[36] B. Lecampion, A. Bunger, and X. Zhang. Numerical methods for hydraulic fracture propagation: A review of recent trends. *Journal of Natural Gas Science and Engineering*, 49:66 – 83, 2018.

[37] S. Lee, M. F. Wheeler, and T. Wick. Pressure and fluid-driven fracture propagation in porous media using an adaptive finite element phase field model. *Computer Methods in Applied Mechanics and Engineering*, 312:509–541, 2016.

[38] S. Lee, M.F. Wheeler, and T. Wick. Pressure and fluid-driven fracture propagation in porous media using an adaptive finite element phase field model. *Computer Methods in Applied Mechanics and Engineering*, 312:509–541, 2016.

[39] S. Lee, M.F. Wheeler, and T. Wick. Pressure and fluid-driven fracture propagation in porous media using an adaptive finite element phase field model. *Computer Methods in Applied Mechanics and Engineering*, 305:111–132, 2016.

[40] S. Lee, M.F. Wheeler, and T. Wick. Iterative coupling of flow, geomechanics and adaptive phase-field fracture including level-set crack width approaches. *Journal of Computational and Applied Mathematics*, 314:40–60, 2017.

[41] T. Li, J.-J. Marigo, D. Guilbaud, and S. Potapov. Gradient damage modeling of brittle fracture in an explicit dynamic context. *International Journal for Numerical Methods in Engineering*, 00(March):1–25, 2016.

[42] J.-J. Marigo, C. Maurini, and K. Pham. An overview of the modelling of fracture by gradient damage models. *Meccanica*, 51(12):3107–3128, 2016.

[43] C. Maurini, B. Bourdin, G. Gauthier, and V. Lazarus. Crack patterns obtained by unidirectional drying of a colloidal suspension in a capillary tube: Experiments and numerical simulations using a two-dimensional variational approach. *International Journal of Fracture*, 184(1-2):75–91, 2013.

[44] C. Miehe, M. Hofacker, L. M. Schänzel, and F. Aldakheel. Phase field modeling of fracture in multi-physics problems. Part II. Coupled brittle-to-ductile failure criteria and crack propagation in thermo-elastic-plastic solids. *Computer Methods in Applied Mechanics and Engineering*, 294:486–522, 2015.

[45] C. Miehe and S. Mauthe. Phase field modeling of fracture in multi-physics problems. Part III. Crack driving forces in hydro-poro-elasticity and hydraulic fracturing of fluid-saturated porous media. *Computer Methods in Applied Mechanics and Engineering*, 304:619–655, 2016.

[46] C. Miehe, S. Mauthe, and S. Teichtmeister. Minimization principles for the coupled problem of Darcy-Biot-type fluid transport in porous media linked to phase field modeling of fracture. *Journal of the Mechanics and Physics of Solids*, 82:186–217, 2015.

[47] A. Mikelić, M.F. Wheeler, and T. Wick. A Phase-Field method for propagating fluid-filled fractures coupled to a surrounding porous medium. *Multiscale Modeling & Simulation*, 48(1):162–186, 2015.

[48] A. Mikelić, M.F. Wheeler, and T. Wick. A quasi-static phase-field approach to pressurized fractures. *Nonlinearity*, 28(5):1371–1399, 2015.

[49] A. Mikelić, M.F. Wheeler, and T. Wick. Phase-field modeling of a fluid-driven fracture in a poroelastic medium. *Computational Geosciences*, 19(6):1171–1195, 2015.

[50] K. Pham, H. Amor, J.-J. Marigo, and C. Maurini. Gradient damage models and their use to approximate brittle fracture. *Int. J. Damage Mech.*, 20(4, SI):618–652, 2011.

[51] D. Santillán, R. Juanes, and L. Cueto-Felgueroso. Phase field model of fluid-driven fracture in elastic media: Immersed-fracture formulation and validation with analytical solutions. *Journal of Geophysical Research: Solid Earth*, 2017.

[52] J.M. Sargado, E. Keilegavlen, I. Berre, and J.M. Nordbotten. High-accuracy phase-field models for brittle fracture based on a new family of degradation functions. *Journal of the Mechanics and Physics of Solids*, 111:458 – 489, 2018.

[53] A. Schlüter, A. Willenbücher, C. Kuhn, and R. Müller. Phase field approximation of dynamic brittle fracture. *Computational Mechanics*, 54(5):1141–1161, 2014.

[54] M. Seiler, P. Hantschke, A. Brosius, and M. Kästner. A numerically efficient phase-field model for fatigue fracture - 1D analysis. *Pamm*, 18(1):e201800207, 2018.

[55] S. Shiozawa, S. Lee, and M.F. Wheeler. The effect of stress boundary conditions on fluid-driven fracture propagation in porous media using a phase-field modeling approach. *International Journal for Numerical and Analytical Methods in Geomechanics*, (February 2018):1–25, 2019.

[56] I.N. Sneddon and M. Lowengrub. *Crack problems in the classical theory of elasticity*. The SIAM series in Applied Mathematics. John Wiley & Sons, 1969.

[57] E. Tanné, T. Li, B. Bourdin, J-J. Marigo, and C. Maurini. Crack nucleation in variational phase-field models of brittle fracture. *J. Mech. Phys. Solids*, 110:80–99, 2018.

[58] C.V. Verhoosel and R. de Borst. A phase-field model for cohesive fracture. *International Journal for Numerical Methods in Engineering*, 00:1–20, 2010.

[59] J. Vignollet, S. May, R. de Borst, and C.V. Verhoosel. Phase-field models for brittle and cohesive fracture. *Meccanica*, 49(11):2587–2601, 2014.

[60] M.F. Wheeler, T. Wick, and W Wollner. An augmented-Lagrangian method for the phase-field approach for pressurized fractures. *Computer Methods in Applied Mechanics and Engineering*, 271:69–85, 2014.

[61] Z.A. Wilson and C.M. Landis. Phase-field modeling of hydraulic fracture. *Journal of the Mechanics and Physics of Solids*, 96:264–290, 2016.

[62] J.-Y. Wu. A unified phase-field theory for the mechanics of damage and quasi-brittle failure. *Journal of the Mechanics and Physics of Solids*, 103:72 – 99, 2017.

[63] K. Yoshioka and B. Bourdin. A variational hydraulic fracturing model coupled to a reservoir simulator. *International Journal of Rock Mechanics and Mining Sciences*, 88:137–150, 2016.

[64] K. Yoshioka, F. Parisio, D. Naumov, R. Lu, O. Kolditz, and T. Nagel. Comparative verification of discrete and smeared numerical approaches for the simulation of hydraulic fracturing. *GEM - International Journal on Geomathematics*, 10(1), 2019.

[65] X. Zhuang, T. Rabczuk, and S. Zhou. A phase-field modeling approach of fracture propagation in poroelastic media. *Engineering Geology*, 2018.